Editors' Suggestion

Antiferromagnetic coupling across nonmagnetic transition-metal films alloyed with ferromagnetic elements

Kevin Winther,[1,*,‖] Zachary R. Nunn,[1,†,‖] Juliana Lisik,[1,‡,‖] Sergiu Arapan,[2,§] Dominik Legut,[2,3] Frank Schulz,[4] Eberhard Goering,[4] Tommy Mckinnon,[1] Spencer Myrtle,[1] and Erol Girt[1,¶]

[1] *Simon Fraser University, 8888 University Drive, Burnaby, British Columbia V5A 1S6, Canada*

[2] *IT4Innovations, VŠB—Technical University of Ostrava, 17 listopadu 3172/15, Ostrava 70800, Czech Republic*

[3] *Department of Condensed Matter Physics, Faculty of Mathematics and Physics, Charles University, Ke Karlovu 3, Prague 2, 121 16, Czech Republic*

[4] *Max Planck Institute for Intelligent Systems, Heisenbergstraße 3, Stuttgart 70569, Germany*

(Received 21 February 2024; revised 22 May 2024; accepted 22 July 2024; published 21 August 2024; corrected 16 September 2024)

Interlayer exchange coupling has been intensively studied for over 30 years and has been successfully incorporated into almost all magnetic thin-film devices. In this study we find that antiferromagnetic interlayer exchange coupling can be achieved across, and improved by, spacer layers containing over 60 at.% of magnetic material. Measurements of sputtered Fe-doped spacer layers with x-ray magnetic circular dichroism reveal that the magnetic atoms in such spacer layers retain a large magnetic moment. The addition of magnetic atoms to the spacer layer is shown to double the coupling strength, leading to the largest-ever-observed antiferromagnetic bilinear coupling strength in magnetic multilayers deposited by magnetron sputtering, which is the industrial technique of choice. Electronic structure calculations in this work predict an experimentally obtained dependence of interlayer exchange coupling on both the magnetic material concentration and the spacer-layer thickness, in contrast with the prevailing understanding of interlayer exchange coupling.

DOI: 10.1103/PhysRevApplied.22.024058

I. INTRODUCTION

Interlayer exchange coupling in metallic multilayers between two ferromagnetic layers across a nonmagnetic spacer layer has been of great interest for fundamental studies and applications. It was discovered in 1986 [1] and found to oscillate between antiferromagnetic and ferromagnetic as a function of the nonmagnetic spacer-layer thickness, d [2–4]. The coupling was observed across the majority of 3d, 4d, and 5d nonmagnetic metallic spacer layers [5]. Interlayer exchange coupling is widely used in spintronic devices to achieve antiferromagnetic coupling between magnetic layers [6]. The advantages of antiferromagnetically coupled magnetic layers, so-called synthetic antiferromagnets, over single ferromagnetic layers are that they have smaller stray magnetic fields and are more difficult to reverse with external magnetic fields and spin-polarized currents [7–9].

In metallic FM|NM|FM transition metal multilayers, where FM is a ferromagnetic layer and NM is a nonmagnetic layer, antiferromagnetic coupling is achieved across nonmagnetic layers only a few atomic layers thick. Thus, the presence of ferromagnetic atoms in NM is hard to avoid due to the difficulty of controlling layer-by-layer deposition. For both fundamental studies and applications, ferromagnetic layers consisting of Co, Co-Fe, and Co-Fe-B coupled across a Ru spacer layer are of particular interest [10]. It has been shown in NMR measurements [11,12] that deposited Co|Ru|Co film structures have interdiffusion between Co and Ru at the Co|Ru interfaces. In the sputtering process, which is the industrial technique of choice for the deposition of magnetic thin films, the high energy of the deposited atoms and neutrals can further accentuate the mixing at the interfaces of these multilayers [11,13,14]. If the enthalpy of formation between the ferromagnetic and nonmagnetic materials is negative, this can also increase mixing at the interfaces. Moreover, magnetic thin-film structures used for devices undergo annealing processes, which can lead to even further intermixing at the interfaces in metallic multilayers [15,16]. For this reason,

*Contact author: kevin_winther@sfu.ca
†Contact author: znunn@sfu.ca
‡Contact author: jbesler@sfu.ca
§Contact author: sergiu.arapan@gmail.com
¶Contact author: egirt@sfu.ca
‖Kevin Winther, Zachary R. Nunn, and Juliana Lisik contributed equally to the paper.

understanding how the presence of ferromagnetic atoms in the spacer layer affects the coupling between ferromagnetic layers is crucial.

To date, there have only been a few studies of antiferromagnetic interlayer exchange coupling across nonmagnetic spacer layers in which ferromagnetic elements are added to the spacer layers in a controlled manner [17,18]. In these studies, Cu noble metal spacer layers were alloyed with ferromagnetic elements. Cu was chosen because detailed theoretical predictions on the oscillation period of coupling across the noble metals Cu, Ag, and Au have been made [19,20]. Alloying was performed to alter the valence electron concentration in the spacer layer while maintaining its nonmagnetic nature, thereby affecting the oscillation period. On the other hand, several recent studies have explored noncollinear interlayer exchange coupling that is between ferromagnetic layers and across spacer layers composed of nonmagnetic transition metals alloyed with ferromagnetic elements [21–23].

Here we present a systematic study of the antiferromagnetic coupling of magnetic Co layers across a RuY transition metal spacer layer, where $Y =$ Co or Fe. RuY spacer layers are good candidates for this study because Co and Fe both form solid solutions with Ru over a large composition range [24]. Additionally, Co|Ru|Co is useful for applications since it has one of the largest reported antiferromagnetic couplings [5].

We will begin by presenting the experimentally measured coupling parameters of Co|RuY|Co structures, exploring various thicknesses and compositions of the RuY spacer layer. Subsequently, we will provide coupling phase diagrams, illustrating the range within which antiferromagnetic coupling can be achieved in Co|RuY|Co. Following this, we will present x-ray magnetic circular dichroism (XMCD) measurements of Co|RuFe|Co, conducted to measure the magnetic moment of Fe atoms in the spacer layer. Electronic structure calculations will then be discussed, aiming to explain the observed experimental results. Finally, a brief discussion of our findings will be offered.

II. METHODS

A. Experimental details

The studied structures, Ta(3.5)|Ru(3.5)|Co(2)| $Ru_{100-x}Y_x(d)$|Co(2)|Ru(3.5) multilayers ($0.4 \leq d \leq 1.6$ nm) and $Ru_{100-x}Y_x(18)$ single films where $Y =$ Co or Fe, are deposited with radiofrequency magnetron sputtering on Si substrates and Si_3N_4 membrane sample chips at room temperature and an argon pressure below 2 mTorr. The numbers in the parentheses represent the layer thicknesses in nanometers. The Ta seed layer is deposited to induce the ⟨0001⟩ growth orientations of the Ru, Co, and $Ru_{100-x}Y_x$ layers, and the top Ru film is used to protect the Co layers from oxidation.

Prior to deposition, Si substrates are cleaned with isopropyl alcohol, followed by the standard RCA SC-1 process, which uses NH_4OH and then H_2O_2 at 343 ± 3 K, to remove particles and organic contaminants. After the cleaning, the Si substrates are rinsed with DI water. Clean substrates and membrane sample chips are first placed in a load lock chamber, which is evacuated to about 5×10^{-7} Torr, and then transferred, without breaking the vacuum, to a process chamber with a base pressure below 5×10^{-8} Torr for deposition. The films are deposited from four elemental 2 in. diameter targets of Ta, Ru, Co, and Fe. The target-to-substrate distance is approximately 8 in. The substrate holder rotates during deposition to ensure thickness and composition uniformity of the deposited films across the substrate surface. The entire sputter process is computer controlled.

A calibration of the growth rates is inferred from fitting x-ray reflectivity measurements of single layers of each material or of Ru(2)|X|Ru(2) multilayers ($X =$ Ta, Co, RuCo, or RuFe) with X'PERT reflectivity software from Panalytical. Large angle x-ray diffraction measurements show that the multilayer structures have strong texture along the ⟨0001⟩ crystallographic orientations with a c-axis full-width-at-half-maximum distribution under 4.8°. The single $Ru_{100-x}Y_x(18)$ films have hcp crystal structure and weak texture along the ⟨0001⟩ crystal directions.

The field dependence of the magnetization, $M(H)$, is measured using a superconducting quantum interference device (SQUID) and vibrating sample magnetometer (VSM) in magnetic fields of up to 7 T and at a temperature of 298 K. Ru$Y(18)$ films are also measured using a SQUID at 10 K.

X-ray magnetic circular dichroism (XMCD) and x-ray absorption spectroscopy (XAS) are measured in total electron yield mode. The sample total drain current signal is normalized by the I_0 signal of a gold grid. An XMCD end station is used, utilizing a superconducting cryogen-free 7-T magnet system, which allows superfast magnetic field ramping rates of up to 1.5 T/s. XMCD measurements are performed at room temperature and in a field above 3 T to ensure that both Co layers are aligned parallel to the external field. All data is corrected for the finite degree of circular polarization. In the regions without XMCD effect, i.e., before and after the edges neglecting magnetic extended x-ray absorption fine-structure (EXAFS) phenomena, offsets are corrected by a single factor, as discussed previously [25]. For the determination of the magnetic moments of Fe, sum rules are applied [26,27], using the number of holes provided for the pure element Fe [28]. Effective electron escape phenomena are estimated by a separate effective electron escape length determined for each phase, i.e., $Ru_{100-x}Fe_x$ ($x = 25$ and 51) and Co, separately [29,30].

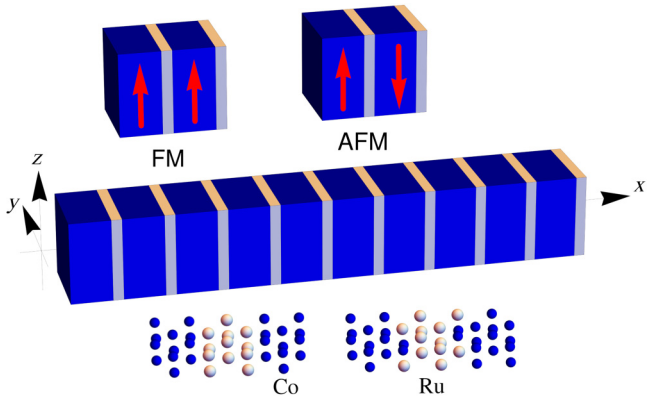

FIG. 1. Schematic representation of calculated Co(2)|Ru(d) structures.

B. Computational details

Electronic structure calculations of $Co_{100-x}Y_x$ (Y = Co or Fe) systems were done with the Vienna *ab initio* simulation package (VASP) software (version 6.2.1). VASP is a plane-wave basis-set implementation [31,32] of the density-functional theory within the projector augmented-wave (PAW) approximation [33]. Calculations were performed using the generalized gradient approximation of Perdew, Burke, and Ernzerhof (PBE) [34] to the exchange-correlation part of the energy functional. We made use of the PAW PBE potentials version 5.4 with 15, 14, and 14 valence electrons for Co, Ru, and Fe, respectively. The size of the plane-wave basis set was determined by an energy cutoff ENCUT = 439.857 eV, which is 50% larger than the default one. The reciprocal space was sampled with a uniform k-point mesh [35] with a separation between k-points KSPACING = 0.1 $Å^{-1}$. For the total energy summation, we used the Methfessel-Paxton method [36], with ISMEAR = 1 and the width of smearing SIGMA = 0.025 eV. The electronic convergence was set to EDIFG = 10^{-7} eV, and geometry optimization was performed until the norms of all of the Hellman-Feynman forces [37] became less than 10^{-3} eV/Å. Equilibrium structure parameters were obtained by performing a set of geometry optimization (ion positions and cell shape) at volumes within a 5% range about equilibrium and fitting the energy vs volume data, $E = E(V)$, to the Rose-Vinet equation of state [38]. Co(2)|Ru(d) multilayers were modeled as periodic supercells of the *hcp* unit cell, with the c axis oriented along the x direction. A supercell comprises two Co layers of about 2 nm (ten Co monolayers) each, separated by a few monolayers of Ru, as shown in Fig. 1.

We estimated the bilinear antiferromagnetic coupling strength J_1 by performing collinear spin-polarized calculations of ferromagnetically and antiferromagnetically coupled Co layers. J_1 is proportional to the energy difference of these two spin configurations, and we calculated it as

$$J_1 = -\frac{E_{\mathrm{AFM}} - E_{\mathrm{FM}}}{2S}, \tag{1}$$

where E_{AFM} and E_{FM} are the energies of the AFM and FM configurations in zero external magnetic field normalized to the number of magnetic ions, and S is the in-plane area of the unit cell. To study the effect on J_1 when substituting Ru atoms with Y = Co or Fe atoms in Co(2.0)|$Ru_{100-x}Y_x$(0.4), we considered a $12 \times 2 \times 2$ supercell with $x = 0, 12.5, 25.0, 37.5, 50.0$. We also utilized a larger $12 \times 3 \times 3$ supercell, and the results are presented within the Supplemental Material [39]. To study the dependence of J_1 on the thickness of spacer layer, d, in Co(2.0)|Ru(d) and Co(2.0)|$Ru_{75}Co_{25}$(d), we considered $(10 + N_{\mathrm{Ru}}) \times 2 \times 2$ supercells, where $N_{\mathrm{Ru}} = 2, 3, 4, 5$ is the number of Ru atomic layers corresponding to spacer-layer thicknesses d = 0.4, 0.6, 0.8, and 1.0 nm, respectively.

C. Coupling model

We used a one-dimensional single-layer micromagnetic model proposed by Eyrich *et al.* [40], and expanded to include J_2 by Nunn *et al.* [21], to fit the field dependence of the magnetization, $M(H)$, of Co|$Ru_{100-x}Y_x$|Co and obtain J_1. The model assumes that the magnetization of Co|$Ru_{100-x}Y_x$|Co is entirely due to the ferromagnetic Co layers.

The model is limited to the experimentally relevant situation in which the external magnetic field is applied parallel to the surface of the films, the ferromagnetic layers have no directional in-plane magnetic anisotropy, and the magnetic moments lie in the plane during magnetization reversal. Additionally, it is presumed that the saturation magnetization, M_s, and exchange stiffness, A_{ex}, do not vary across the ferromagnetic layers.

In our multilayers, the uniaxial magnetocrystalline anisotropy field of the Co layers is along the ⟨0001⟩ directions, perpendicular to the Co film plane. The demagnetizing dipolar field in Co films is much larger than the uniaxial magnetocrystalline anisotropy field, forcing the magnetization to lie in the plane of the film. Due to the polycrystalline nature of the studied samples, the in-plane magnetocrystalline anisotropy is averaged. In this case, the anisotropy and demagnetization energies can be neglected in calculating the total magnetic energy. In Eyrich's model, the total magnetic energy is written as the sum of the Zeeman, exchange interaction, and interlayer exchange coupling energies of the ferromagnetic Co layers. The interlayer exchange coupling energy at zero applied magnetic field is written as [21]

$$E_{\mathrm{coupling}} = J_1 \cos(\theta) + J_2 \cos^2(\theta), \tag{2}$$

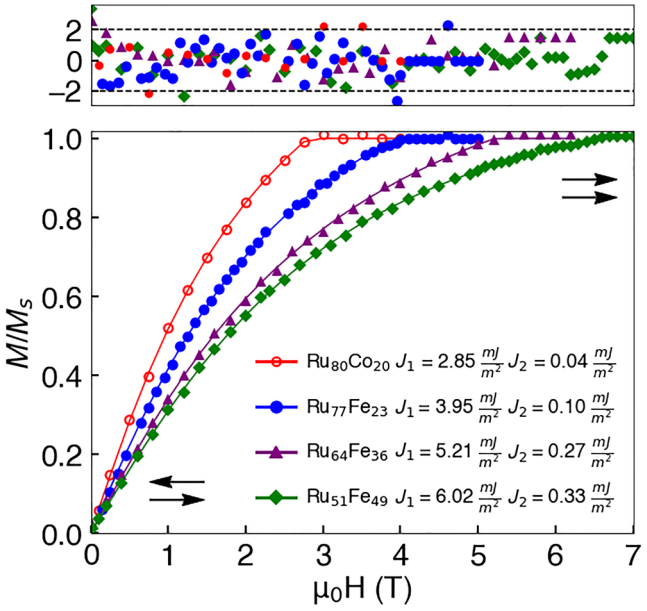

FIG. 2. Normalized magnetization as a function of magnetic field measurements, $M(H)$, of Co(2)|$Ru_{80}Co_{20}$(0.45)|Co(2) and Co(2)|$Ru_{100-x}Fe_x$(0.45)|Co(2) where $A = 17$ pJ/m, $M_s = 1350$ kA/m, and $x = 23$, 36, and 49. Solid lines represent simulations of $M(H)$ data using the model proposed by Eyrich *et al.* [40] Magnetic moments of Co films are antiferromagnetic at zero field and ferromagnetic at fields for which $M/M_s = 1$. Normalized residuals (residuals divided by the standard deviation) are plotted above.

where J_1 and J_2 are the bilinear and biquadratic coupling strengths, respectively, and θ is the zero-field coupling angle between the magnetic moments of the ferromagnetic layers [41]. J_1 accounts for the strength of antiferromagnetic coupling ($\theta = 180°$) if $J_1 > 0$ and ferromagnetic coupling ($\theta = 0°$) if $J_1 < 0$. J_2 is always positive in our structures and accounts for the strength of orthogonal coupling ($\theta = 90°$). The emphasis of this work is on antiferromagnetic coupling, which occurs when $J_1 > 2J_2$ and $\theta = 180°$. Examples of experimental data with fits using the above model can be found in Fig. 2.

III. RESULTS AND DISCUSSION

A. Antiferromagnetic coupling parameters

Figures 3(a) and 3(b) shows J_1 and J_2 of Co(2)|$Ru_{100-x}Co_x(d)$|Co(2) as a function of d and x. The interlayer exchange coupling of the Co layers across Ru in Co|Ru(d)|Co is antiferromagnetic for $0.35 \leq d \leq 1.0$ nm. J_1 of Co|Ru(d)|Co oscillates and its maxima decrease as $1/d^2$, in agreement with previous reports [3,42]. This $1/d^2$ dependence is represented by the gray line in Fig. 3(a). The interface reflection model proposed by Stiles [43] and Bruno [44] was employed by Mckinnon *et al.* [45] to fit the dependence of J_1 on Ru spacer layer thickness for Co|Ru(d)|Co films.

The addition of Co to the Ru spacer layer damps the oscillations of J_1 while lowering the magnitude of the J_1 maxima as seen in Fig. 3(a). For x larger than about 37, the oscillations are barely present and J_1 initially increases with d and then closely follows the $1/d^2$ dependence represented by the gray line. It is worthwhile to note that, for Co concentrations of approximately 20 at.%, the magnitude of J_1 is almost constant for $0.6 \leq d \leq 1.0$ nm. This is attractive for the fabrication of thin-film devices, as the thickness of the spacer layer does not need to be precisely controlled.

J_2 of Co|RuCo|Co, on the other hand, is smaller than approximately 0.1 mJ/m^2 for $x \leq 20$ [Fig. 3(b)]. For $x \geq 37$, J_2 increases with decreasing d and eventually becomes large enough to produce noncollinear coupling. This noncollinear coupling data is not included here for J_2 and is further discussed in our previous work [23].

Figures 3(c) and 3(d) show J_1 and J_2 of Co(2)|$Ru_{100-x}Fe_x(d)$|Co(2) as a function of d and x. The first maximum of J_1, which occurs at $d = 0.4$ nm, increases with the addition of Fe to the Ru spacer layer until the atomic concentration reaches $x = 49$. The $M(H)$ curves of Co(2)|$Ru_{100-x}Fe_x$(0.45)|Co(2) for $x = 23$ to 49, which show a rapid increase of the saturation field with x, are presented in Fig. 2 in Part C of the Sec. II. At $x = 49$, the maximum of J_1, $J_1 = 6.9 \pm 0.3$ mJ/m^2, is twice as large as it is for the pure Ru spacer layer. This is the largest antiferromagnetic interlayer exchange coupling strength ever observed in metallic multilayers deposited by sputtering.

Previously, the highest experimentally obtained J_1 value for Co|Ru|Co multilayers, deposited via sputtering, was 5 mJ/m^2 at 300 K [3]. Additionally, there is one report of an even larger value of $J_1 = 34$ mJ/m^2 observed in Co|Rh|Co multilayers obtained using e-beam deposition onto a substrate held at room temperature [14]. As previously mentioned, the sputtering process involves high-energy deposition of atoms and neutrals, leading to enhanced mixing at the interfaces of multilayered thin films. This makes achieving layer-by-layer deposition challenging. In contrast, Co|Rh|Co multilayers were deposited using the e-beam technique, which deposits atoms at much lower energy than sputter deposition, minimizing interface mixing in the deposited multilayers. This could explain the much larger coupling achieved using this deposition technique. The largest J_1 value obtained in Co|Rh|Co multilayers using sputter deposition was 1.6 mJ/m^2 [3].

The oscillation of J_1 persists with the addition of up to 70 at.% of Fe in Ru, with practically the same oscillation period as in Co|Ru|Co. For $x \leq 49$, J_2 of Co|RuFe|Co peaks between 0.45 and 0.5 nm and remains below approximately 0.35 mJ/m^2 [Fig. 3(d)]. For $x \geq 62$, J_2 increases with decreasing d and eventually becomes large enough to

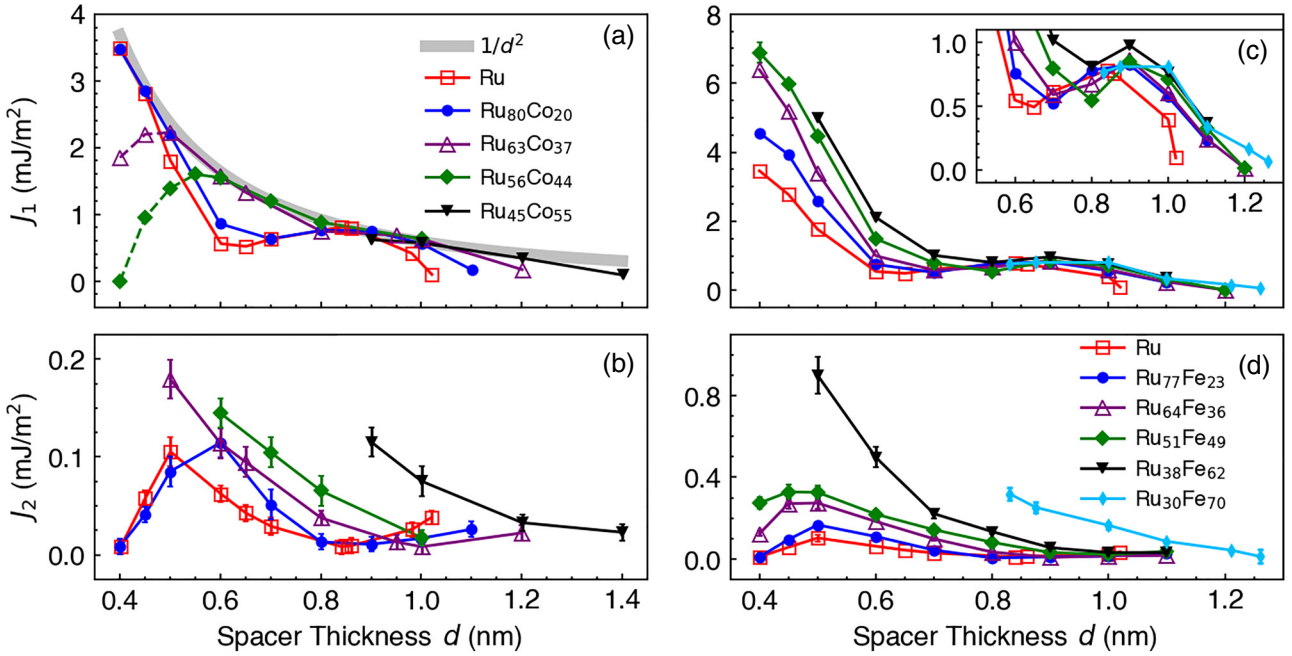

FIG. 3. The experimentally determined dependence of (a) J_1 and (b) J_2 of Co(2)|$Ru_{100-x}Co_x(d)$|Co(2), and (c) J_1 and (d) J_2 of Co(2)|$Ru_{100-x}Fe_x(d)$|Co(2) on the spacer-layer thickness, d. The inset plot in (c) is the enlarged J_1 versus d dependence for $0.5 \leq d \leq 1.3$ nm. A broad, gray line with $1/d^2$ dependence is added to (a) for comparison. J_1 values for Co(2)|$Ru_{100-x}Co_x(d)$|Co(2), where $x = 37$ and 44, and $d \leq 0.5$ nm are from Nunn *et al.* [23]. Both solid and dotted lines that connect the experimental data in the figure are drawn to guide the eye. Measurements are performed at 298 K.

produce noncollinear coupling [46]. The observed J_2 values for coupling across RuFe are several times larger than those for coupling across RuCo.

B. Coupling phase diagrams

The coupling in Co|Ru(d)|Co oscillates and rapidly decreases in strength with increasing d [47]. The first antiferromagnetic coupling region occurs over a wide d range, $0.35 \leq d \leq 1.0$ nm. This is the only antiferromagnetic region of interest for applications, primarily due to its large coupling strength. The coupling phase diagrams in Figs. 4(a) and 4(b) show how this region, which is the focus of this study, evolves with the addition of Co and Fe, respectively. These regions are shaded to be easily identified.

Antiferromagnetic coupling between Co layers in Co|$Ru_{100-x}Co_x(d)$|Co can be achieved for $x \leq 60$ [Fig. 4(a)]. As the concentration of Co in the Ru spacer layer increases, the first antiferromagnetic region shifts to higher d values. The breadth of the region remains unchanged for x between 0 and 40 and is reduced for $x > 50$.

The saturation magnetization, M_s, of 18-nm-thick $Ru_{100-x}Co_x$ films is measured at room temperature and at 10 K as a function of x [Fig. 4(a)]. At room temperature, the M_s of $Ru_{100-x}Co_x$ films is zero for x between 0 and 55 and sharply increases for x larger than 60. At the same concentration for which M_s of RuCo(18) begins to increase sharply ($x = 60$), the coupling of Co|RuCo|Co ceases to be antiferromagnetic. The sharp increase in M_s is associated with the onset of ferromagnetism in the RuCo alloy, which is responsible for the loss of antiferromagnetic coupling in Co|RuCo|Co [23]. The M_s measurements at 10 K show that $Ru_{100-x}Co_x$ spacer layers have a Curie temperature between 10 and 298 K for $44 \leq x \leq 60$. This suggests that antiferromagnetic coupling can be achieved across paramagnetic spacer layers that at low temperatures exhibit a ferromagnetic-to-paramagnetic transition.

Antiferromagnetic coupling in Co|$Ru_{100-x}Fe_x$|Co can be achieved over a wider x range, $x \leq 74$, as shown in Fig. 4(b). As the concentration of Fe in the Ru spacer layer increases, the lower d bound of the first antiferromagnetic region remains the same until $x = 50$ and then increases with x. The breadth of the region increases with x for $x < 23$, stays constant for x between 23 and 50, and decreases with further increase of x.

The saturation magnetization measurements of 18-nm-thick $Ru_{100-x}Fe_x$ films as a function of x are also included in Fig. 4(b). The M_s dependence on x of the RuFe films is the same at both 10 K and room temperature. M_s is zero for $x \leq 74$ and sharply increases for $x \geq 77$. The increase in M_s coincides with the loss of antiferromagnetic coupling in Co|$Ru_{100-x}Fe_x$|Co.

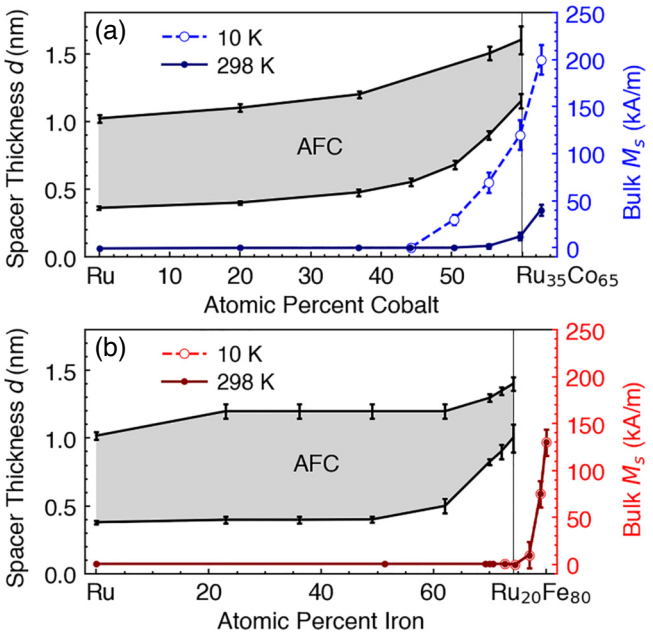

FIG. 4. Coupling phase diagram showing the first antiferromagnetic coupling region of (a) Co|$Ru_{100-x}Co_x(d)$|Co and (b) Co|$Ru_{100-x}Fe_x(d)$|Co as a function of spacer-layer thickness, d, and ferromagnetic element concentration, x, at 298 K. M_s of 18-nm-thick single $Ru_{100-x}Y_x$ layer as a function of x over the same x range is also included for 10 and 298 K.

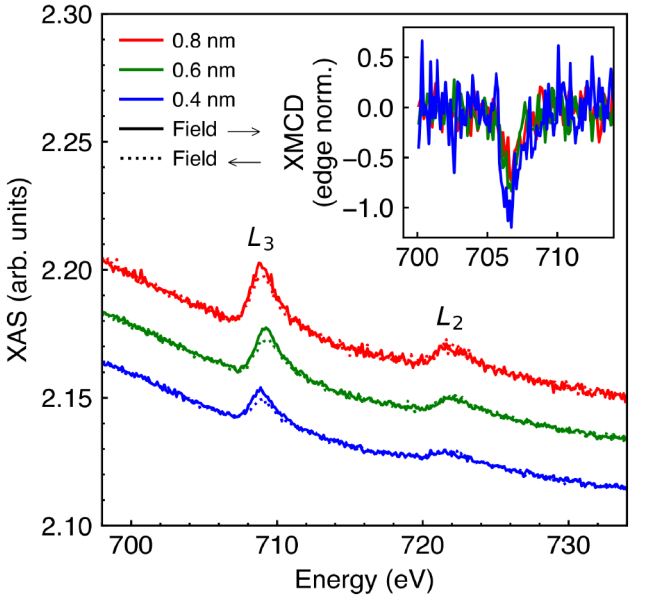

FIG. 5. Non-edge-normalized XAS spectra near the Fe $L_{2,3}$ edges of Co(5)|$Ru_{75}Fe_{25}(d)$|Co(2.5) samples. The inset shows the respective edge-normalized XMCD signal around the L_3 peak.

C. X-ray magnetic circular dichroism (XMCD)

X-ray absorption spectroscopy (XAS) measurements yield element-specific information by probing a sample with photons at energies that correspond to the electronic energy levels of a certain atomic species. Combined with the x-ray magnetic circular dichroism (XMCD) effect, the magnetic properties of certain atomic species can be probed individually. Using XMCD sum rules [28], it is possible to obtain quantitative information about the orbital and spin contributions of the magnetic moment per atom of a certain element.

This method is used in order to study the magnetic properties of Fe added to the Ru spacer layer in a Ta|Ru|Co(5)|$Ru_{75}Fe_{25}(d)$|Co(2.5)|Ru film with $d = 0.4$, 0.6 and 0.8 nm. The data, presented in Fig. 5, shows the raw XAS spectra, normalized to the beam intensity that is monitored by an Au-coated Cu grid. Depicted are the Fe $L_{2,3}$ edges with the magnetic field applied parallel (solid line) and antiparallel (dotted line) to the vector of circular polarization. The spectra for each spacer-layer thickness, d, is shifted along the y axis to allow for better comparison.

It is evident that the overall signal decreases for thinner spacer layers, due to the reduced total amount of Fe in the samples. While an XMCD effect is clearly visible at the L_3 edge (difference between solid line, field applied parallel, and dotted line, field applied anti-parallel), it seems to vanish at the L_2 edge, indicating an increased orbital magnetic moment with respect to bulk Fe [27].

The edge-normalized XMCD spectra around the L_3 peak shown in the inset of Fig. 5 reveal that the averaged magnetic moment per Fe atom increases for thinner spacer layers. From the edge-normalized spectra, the magnetic moment per Fe atom is calculated according to the Fe $L_{2,3}$ edge sum rules. The results are shown in Table I, including the orbital contribution m_l, the spin contribution m_s, and the total magnetic moment m_{tot}. The values for m_{tot} decrease from $1.26\mu_B$ to $0.87\mu_B$ with increasing d from 0.4 to 0.8 nm, while the orbital contribution does not change significantly.

The 0.4-nm spacer layer is only two atomic layers thick, meaning that every Fe atom in the RuFe spacer layer is expected to be in direct contact with Co atoms from the surrounding magnetic layers. This polarizes the Fe atoms in the spacer layer, giving them a large magnetic moment. At 0.6 nm (three atomic layers) and 0.8 nm (four

TABLE I. XMCD sum-rule results for orbital, m_l, spin, m_s, and total magnetic moment, m_{tot}, of the Fe $L_{2,3}$ edge in Co(5)|$Ru_{75}Fe_{25}(d)$|Co(2.5) samples.

d [nm]	m_l	m_s	m_{tot}
0.4	0.13	1.13	1.26
0.6	0.16	0.95	1.11
0.8	0.16	0.71	0.87

atomic layers), not all Fe atoms have to be in direct contact with Co atoms and the total magnetic moment per Fe atom decreases monotonically. This indicates that not all Fe atoms have the same moment but instead that the Fe atoms in direct contact with the surrounding Co layers are strongly polarized, while the Fe atoms not in direct contact with the Co layers are less polarized. It is also clear that this polarization is not a pure interface effect as, if it were, the magnetic moment per Fe atom would be halved when doubling the spacer-layer thickness, which is not the case.

D. Calculations and comparisons to experiment

The experimental results in Fig. 3 show that J_1 in Co|Ru(d)|Co structures oscillates as the spacer-layer thickness, d, increases. These oscillations persist with the addition of Fe to the spacer layer but are damped with the addition of Co, following a $1/d^2$ dependence. Furthermore, in structures where $d = 0.4$ nm (two atomic layers thick), J_1 strongly increases with the addition of Fe to a maximum of 6.9 ± 0.3 mJ/m^2. Contrarily, the addition of Co causes J_1 to decrease monotonically until antiferromagnetic coupling can no longer be achieved. To explain the differences caused by the presence of these two magnetic materials in the Ru spacer layer, electronic structure calculations using the Vienna *ab initio* simulation package (VASP) software are presented alongside experimental results in Figs. 6 and 7.

Calculations of J_1 in Co|Ru$_{100-x}Y_x(d)$|Co structures are dependent on the distribution of Y atoms in the spacer layer. For this reason, the atomic structures used in the calculations for $d = 0.4$ nm are depicted alongside the results in the figures. Additional atomic structures for larger values of d, also utilized in the presented calculations, are included within the Supplemental Material [39].

In Fig. 6(a), the experimental J_1 dependence on spacer-layer thickness, d, for Co|Ru(d)|Co structures is compared to two calculations. The first calculation, structure A, assumes atomically sharp Co|Ru interfaces without Co-Ru intermixing. The second calculation, structure B, assumes that the Co|Ru interface layers contain the same amount of Co and Ru atoms. Calculations show that for both A and B structures, J_1 oscillates with a dependence on d, even changing sign at $d = 0.6$ nm and $d = 1.05$ nm for atomically sharp interfaces, structure A. However, the intermixing of Co and Ru at the interface, in structure B, damps the oscillations, resulting in the positive values of J_1 for all calculated d values. Thus, comparing experimental results to the calculations could indicate some intermixing at the Co|Ru interfaces in the sputter-deposited samples.

In Fig. 6(b), experimental results for the Co|Ru$_{63}$Co$_{37}$(d)|Co structure are compared to calculations obtained assuming two different Co|Ru$_{75}$Co$_{25}$(d)|Co structures, labeled C and D. In structure C, at least one atomic layer of the Ru$_{75}$Co$_{25}$ spacer layer is composed of only

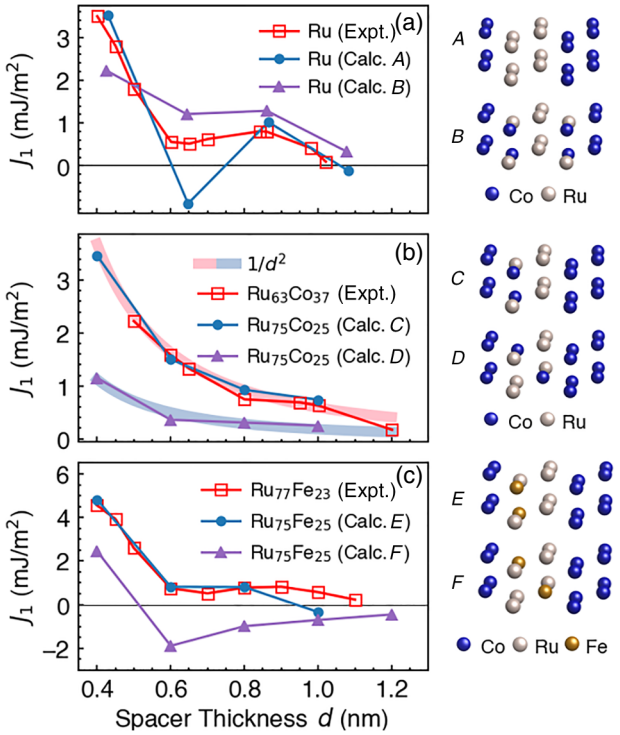

FIG. 6. J_1 as a function of spacer-layer thickness, d of (a) Co|Ru(d)|Co, (b) Co|Ru$_{100-x}$Co$_x$(d)|Co, and (c) Co|Ru$_{100-x}$Fe$_x$(d)|Co. Two broad red and blue lines with $1/d^2$ dependence are added to (b) for comparison. Structures used in calculations are provided to the right of the plot for $d = 0.4$ nm.

Ru atoms with the remaining Co atoms grouping around the interfaces. In structure D, Co atoms are uniformly distributed throughout the Ru$_{75}$Co$_{25}$ spacer layer. Adding Co to the Ru spacer layer effectively increases the Ru-Co intermixing. As a result, for both calculated structures, the J_1 oscillations are completely damped. Additionally, both calculations follow a $1/d^2$ dependence, the same as observed in the experimental data for Co|Ru$_{100-x}$Co$_x$|Co with $x \geq 37$ and in the range of the RuCo spacer-layer thickness for which the coupling is antiferromagnetic [Fig. 4(a)].

In Fig. 6(c), the dependence of J_1 on the spacer-layer thickness, d, is explored in Co|Ru$_{100-x}$Fe$_x$|Co structures by comparing the experimental results when $x = 23$ to the calculated atomic structures, E and F, where $x = 25$. The structures E and F are the same as the structures C and D but with the Co atoms in the spacer layer substituted for Fe atoms. Both calculations exhibit oscillations in J_1 consistent with experimental results. Additionally, there is agreement between the experimental data and calculations obtained from structure E from $d = 0.4$ nm to 0.8 nm. At $d = 1.0$ nm, the calculation deviates from the experimental data. In our calculations, only a few generic distributions of Fe atoms in the spacer layer are tested for $d = 1.0$ nm out of the many combinations that could occur, which could explain the observed discrepancy.

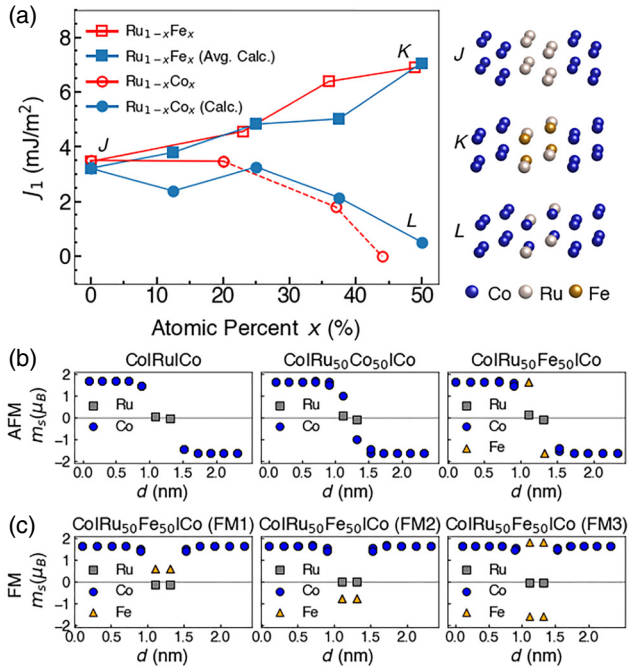

FIG. 7. The dependence of experimentally determined and calculated values of J_1 on atomic concentration, x, for $Y = \mathrm{Fe}$ and Co, in $\mathrm{Co|Ru_{100-x}}Y_x(0.4)\mathrm{|Co}$. The experimental J_1 values for $\mathrm{Co|Ru_{100-x}Co_x(0.4)|Co}$ ($x \geq 37$) are taken from Nunn *et al.* [23]. Selected structures used for the calculations are depicted on the right of the plot and labeled J (Co|Ru|Co), K (Co|Ru$_{50}$Fe$_{50}$|Co), and L (Co|Ru$_{50}$Co$_{50}$|Co). The magnetic moments of Co, Fe, and Ru atoms are shown below in the case of antiferromagnetic alignment of the Co layers for structures J, K, and L (labeled AFM) and the case of ferromagnetic alignment of the Co layers for three possible magnetic alignments of Fe in the structure K (labeled FM).

The results presented in Fig. 6 demonstrate that the electronic structure calculations can predict the dependence of J_1 on the spacer-layer thickness in $\mathrm{Co|Ru_{100-x}}Y_x\mathrm{|Co}$.

In the studied magnetic multilayer structures with only two atomic layer thick spacer layers ($\mathrm{Co|Ru_{100-x}}Y_x(0.4)\mathrm{|Co}$), the magnitude of J_1 strongly depends on the concentration of the magnetic element Y in the spacer layer. This is shown in Fig. 7(a) where experimental values and calculations of J_1 are compared for atomic concentrations of $x \leq 50$. For $\mathrm{Co|Ru_{100-x}Co_x(0.4)|Co}$ structures with $x \geq 37$, the coupling between Co layers is noncollinear and, as such, J_1 values are taken from Nunn *et al.* [23]. Atomic structures J, K, and L used for calculations are depicted alongside the results in Fig. 7(a). The structures assume atomically sharp Co|Ru interfaces without Co-Ru intermixing. The structures K and L are similar to structure J, with one, two, three, or four atoms of Ru in the spacer layer substituted with either Co or Fe atoms to achieve the composition of $\mathrm{Ru_{100-x}}Y_x$ with $x = 12.5$, 25, 37.5, or 50.

J_1 is calculated from the difference between the energies in the case of antiferromagnetic, AFM, and ferromagnetic, FM, magnetization alignments of the Co layers in the studied multilayers. For both the AF and FM magnetization alignments the magnetic moments of Ru and Y atoms in the spacer layer and Co atoms in the surrounding Co layers are plotted against layer thickness in Figs. 7(b) and 7(c). In the case of antiferromagnetic alignment of Co layers in $\mathrm{Co|Ru_{100-x}}Y_x(0.4)\mathrm{|Co}$, the magnetic moments of both Co and Fe atoms in the $\mathrm{Ru_{100-x}}Y_x$ spacer layer align ferromagnetically to the neighboring Co layer, as depicted in Fig. 7(b).

In contrast, in the case of ferromagnetic alignment of Co layers in $\mathrm{Co|Ru_{100-x}}Y_x(0.4)\mathrm{|Co}$, the calculations suggest that the magnetic moments of Co and Fe atoms in the $\mathrm{Ru_{100-x}}Y_x$ spacer layer may exhibit different magnetic alignments. In $\mathrm{Co|Ru_{100-x}Co_x(0.4)|Co}$ structures, the magnetic moments of Co atoms in the RuCo spacer layer align ferromagnetically to the neighboring Co layers. In contrast, in $\mathrm{Co|Ru_{100-x}Fe_x(0.4)|Co}$ structures, the magnetic moments of Fe atoms in the RuFe spacer layer can assume three different magnetic configurations with similar energy. These three configurations are illustrated in Fig. 7(c), where the magnetic moments of Fe in the spacer layer align either ferromagnetically to the Co layers (FM1), antiferromagnetically to the Co layers (FM2), or both ferromagnetically and antiferromagnetically to the Co layers (FM3). Consequently, in $\mathrm{Co|Ru_{100-x}Fe_x(0.4)|Co}$, J_1 is determined by averaging the bilinear coupling obtained from all three magnetic configurations. The calculations are performed in the absence of an external magnetic field.

It is clear from Fig. 7(a) that the theoretical calculations can predict the experimental data. The addition of Fe to the Ru spacer layer increases antiferromagnetic coupling strength while the addition of Co to the Ru spacer layer decreases the strength of antiferromagnetic coupling.

In Table II, the mean absolute magnetic moments of Co atoms at $\mathrm{Co|Ru_{100-x}}Y_x$ interfaces, $m_{s,\mathrm{Int}}^{(Co)}$, and Y atoms in the Ru$Y$ spacer layer, $m_{s,\mathrm{SL}}^{(Y)}$, in $\mathrm{Co|Ru_{100-x}}Y_x(0.4)\mathrm{|Co}$ structures are presented for the case of ferromagnetic alignment of Co layers. The values of $m_{s,\mathrm{SL}}^{(\mathrm{Fe})}$ are determined from the three magnetic structures illustrated in Fig. 7(c). Here, $m_{s,\mathrm{SL}}^{(\mathrm{Fe1})}$, $m_{s,\mathrm{SL}}^{(\mathrm{Fe2})}$, and $m_{s,\mathrm{SL}}^{(\mathrm{Fe3})}$ represent the mean absolute magnetic moments of Fe atoms in the FM1, FM2, and FM3 structures, respectively. On the other hand, $m_{s,\mathrm{SL}}^{(\mathrm{Co})}$ is calculated from the lowest energy state structure, where the magnetic moments of Co atoms in the spacer layer are aligned ferromagnetically with the magnetic moments of the Co layers. $m_{s,\mathrm{SL}}^{(\mathrm{Fe3})}$ for $x = 12.5$ is not listed in the table since, in this case, only one Fe atom is in the spacer layer with its magnetic moment oriented ferromagnetically (FM1) or antiferromagnetically (FM2) to the magnetic moments of the surrounding Co layers.

TABLE II. Average of the absolute values of the magnetic moments of the Co atoms at the Co|$Ru_{100-x}Y_x$ interfaces, $m_{s,\mathrm{Int}}^{(\mathrm{Co})}$, and Y atoms in the RuY spacer layer, $m_{s,\mathrm{SL}}^{(Y)}$, calculated for ferromagnetic alignment of Co layers in Co|$Ru_{100-x}Y_x(0.4)$|Co. $m_{s,\mathrm{SL}}^{(\mathrm{Fe1})}$, $m_{s,\mathrm{SL}}^{(\mathrm{Fe2})}$ and $m_{s,\mathrm{SL}}^{(\mathrm{Fe3})}$ are the magnetic moments of Fe atoms in the RuFe spacer layer of FM1, FM2, and FM3 structures, respectively. All magnetic moments are calculated in units of μ_B in the absence of an external magnetic field.

FM	$Y=$ Co			$Y=$ Fe		
x [%]	$m_{s,\mathrm{Int}}^{(\mathrm{Co})}$	$m_{s,\mathrm{SL}}^{(\mathrm{Co})}$	$m_{s,\mathrm{Int}}^{(\mathrm{Co})}$	$m_{s,\mathrm{SL}}^{(\mathrm{Fe1})}$	$m_{s,\mathrm{SL}}^{(\mathrm{Fe2})}$	$m_{s,\mathrm{SL}}^{(\mathrm{Fe3})}$
0	1.46					
12.5	1.53	0.65	1.49	1.68	1.56	
25.0	1.56	0.80	1.50	1.39	1.32	1.54
37.5	1.56	0.86	1.50	1.27	1.04	1.67
50.0	1.54	0.89	1.50	0.62	0.79	1.71

Table III summarizes the $m_{s,\mathrm{Int}}^{(\mathrm{Co})}$ and $m_{s,\mathrm{SL}}^{(Y)}$ values calculated for antiferromagnetic alignment of Co layers in Co|$Ru_{100-x}Y_x(0.4)$|Co. $m_{s,\mathrm{SL}}^{(Y)}$ data are calculated from the lowest energy state as depicted in Fig. 7(b). In all investigated Co|$Ru_{100-x}Y_x(0.4)$|Co structures, the magnetic moments of Ru atoms in the spacer layer are less than $0.1\mu_B$ and are consequently not listed in the tables.

In the Co|Ru|Co structure J, the mean absolute magnetic moment of Co atoms at the Co|Ru interfaces, $m_{s,\mathrm{Int}}^{(\mathrm{Co})}$, decreases by approximately 12%, from 1.67 to $1.46\mu_B$, when the magnetic moments of the Co layers are either ferromagnetically (FM) or antiferromagnetically (AFM) aligned. This trend is observed in all the calculated $d=0.4$ nm structures and is in agreement with the results from Eyrich *et al.* [48], which shows that Ru atoms reduce the magnetic moments of neighboring Co atoms in CoRu alloys.

As Co atoms are introduced to the spacer layer, illustrated by the Co|$Ru_{50}Co_{50}$|Co structure L, a similar effect occurs. Co atoms in the spacer layer exhibit decreased magnetic moments of $1.00\mu_B$ for ferromagnetic (FM) and $0.89\mu_B$ for antiferromagnetic (AFM) Co layer alignments, attributed to neighboring Ru atoms. As a consequence of the addition of Co to the spacer layer, the Co atoms in the magnetic layers at the Co|RuCo interfaces see an increased average magnetic moment from $1.46\mu_B$ for $x=0$ to 1.54 and $1.55\mu_B$ for $x=50$ for AFM and FM Co layer alignments, respectively. This can be also explained by the reduced number of neighboring Ru atoms.

TABLE III. Average of the absolute values of the magnetic moments of the Co atoms at the Co|$Ru_{100-x}Y_x$ interfaces, $m_{s,\mathrm{Int}}^{(\mathrm{Co})}$, and Y atoms in the RuY spacer layer, $m_{s,\mathrm{SL}}^{(Y)}$, calculated for antiferromagnetic alignment of Co layers in Co|$Ru_{100-x}Y_x(0.4)$|Co. All magnetic moments are calculated in units of μ_B in the absence of an external magnetic field.

AFM	$Y=$ Co		$Y=$ Fe	
x [%]	$m_{s,\mathrm{Int}}^{(\mathrm{Co})}$	$m_{s,\mathrm{SL}}^{(\mathrm{Co})}$	$m_{s,\mathrm{Int}}^{(\mathrm{Co})}$	$m_{s,\mathrm{SL}}^{(\mathrm{Fe})}$
0	1.46			
12.5	1.52	0.73	1.48	1.70
25.0	1.56	1.01	1.49	1.58
37.5	1.56	0.88	1.49	1.58
50.0	1.55	1.00	1.50	1.64

Similarly, regardless of alignment, Fe atoms in the spacer layer also experience a reduced magnetic moment due to the neighboring Ru atoms. Although the mean absolute magnetic moment of Fe atoms is reduced, it is still greater than that of the Co atoms in the spacer layers. In the case of the ferromagnetic alignment of Co layers, the mean absolute magnetic moment of Fe atoms, across all three structures (FM1, FM2, and FM3), ranges from $1.62\mu_B$ for $x=12.5$ to $1.04\mu_B$ for $x=50$, as seen in Table II. On the other hand, in the case of the antiferromagnetic alignment of Co layers, the mean absolute magnetic moment of Fe atoms ranges from $1.70\mu_B$ for $x=12.5$ to $1.64\mu_B$ for $x=50$, as seen in Table III.

With the addition of Fe atoms to the spacer layer, the average magnetic moment of Co atoms in the magnetic layers at the Co|RuFe interfaces show an increase with x from $1.46\mu_B$ at $x=0$ to $1.50\mu_B$ at $x=50$ for both alignments of Co layers. As in Co|RuCo|Co structures, this increase can be attributed to the reduced number of neighboring Ru atoms.

From the above results, it can be concluded that in $d=0.4$ nm structures the addition of Y atoms to the spacer layer increases the magnetic moment of Co atoms in the magnetic layers at Co|RuY interfaces. Additionally, Fe atoms in the spacer layer have a greater average magnetic moment than Co atoms in the spacer layer. In the case of the ferromagnetic alignment of Co layers, Co atoms in the spacer layer always align ferromagnetically to neighboring Co layers. On the other hand, Fe atoms can have three different alignments with the FM3 structure [see Fig. 7(c)] having the lowest energy for $x>25$ and the FM2 structure having the lowest energy for $x\leq 25$ in the 0.4-nm-thick RuFe spacer layers.

IV. SUMMARY

Our research shows that the addition of magnetic materials to nonmagnetic spacer layers in Co(2)|$Ru_{100-x}Y_x(d)$|Co(2) structures ($Y=$ Co or Fe) can cause the antiferromagnetic coupling strength to vary drastically based on the atomic concentration of Co or Fe in the spacer layer. It was found that the addition of Co to the spacer layer causes the bilinear coupling constant, J_1, to exhibit damped oscillations that follow a $1/d^2$ dependence. It was observed that the addition of Fe to the spacer layer significantly enhances J_1 while retaining its oscillations with d. The maximum concentrations of Co and Fe in the spacer layer,

at which antiferromagnetic coupling is achieved in these structures, are at 60 and 74 at.%, respectively. For the thinnest studied spacer layers ($d = 0.4$ nm), increasing the Fe concentration results in a doubling of the magnitude of J_1: from $J_1 = 3.5 \pm 0.3$ mJ/m^2 for $x = 0$ to $J_1 = 6.9 \pm 0.3$ mJ/m^2 for $x = 50$. This is the largest antiferromagnetic interlayer exchange coupling strength ever to be observed in metallic multilayers deposited by sputtering. In contrast, the addition of Co to the spacer layer causes J_1 to decrease monotonically. These findings are supported through electronic structure calculations.

XMCD data of Ta|Ru|Co(5)|$Ru_{75}Fe_{25}(d)$|Co(2.5)|Ru structures show that Fe atoms in the spacer layer are strongly polarized. These findings are also supported by electronic structure calculations.

ACKNOWLEDGMENTS

The authors acknowledge financial support from the Natural Sciences and Engineering Research Council of Canada (NSERC), the Czech Science Foundation, Project No. 22-35410K and the projects e-INFRA CZ (ID:90254) and QM4ST No. CZ.02.01.01/00/22_008/0004572 by the Ministry of Education, Youth and Sports of the Czech Republic. The authors would also like to thank George Lertzman-Lepofsky for his assistance with editing.

[1] P. Grünberg, R. Schreiber, Y. Pang, M. B. Brodsky, and H. Sowers, Layered magnetic structures: Evidence for antiferromagnetic coupling of Fe layers across Cr interlayers, Phys. Rev. Lett. **57**, 2442 (1986).

[2] B. Heinrich, Z. Celinski, J. F. Cochran, W. B. Muir, J. Rudd, Q. M. Zhong, A. S. Arrott, K. Myrtle, and J. Kirschner, Ferromagnetic and antiferromagnetic exchange coupling in bcc epitaxial ultrathin Fe(001)/Cu(001)Fe(001) trilayers, Phys. Rev. Lett. **64**, 673 (1990).

[3] S. S. P. Parkin, N. More, and K. P. Roche, Oscillations in exchange coupling and magnetoresistance in metallic superlattice structures: Co/Ru, Co/Cr, and Fe/Cr, Phys. Rev. Lett. **64**, 2304 (1990).

[4] J. E. Ortega, F. J. Himpsel, G. J. Mankey, and R. F. Willis, Quantum-well states and magnetic coupling between ferromagnets through a noble-metal layer, Phys. Rev. B **47**, 1540 (1993).

[5] S. S. P. Parkin, Systematic variation of the strength and oscillation period of indirect magnetic exchange coupling through the 3*d*, 4*d*, and 5*d* transition metals, Phys. Rev. Lett. **67**, 3598 (1991).

[6] R. A. Duine, K.-J. Lee, S. S. P. Parkin, and M. D. Stiles, Synthetic antiferromagnetic spintronics, Nat. Phys. **14**, 217 (2018).

[7] I. Tudosa, J. A. Katine, S. Mangin, and E. E. Fullerton, Perpendicular spin-torque switching with a synthetic antiferromagnetic reference layer, Appl. Phys. Lett. **96**, 212504 (2010).

[8] M. Arora, C. Fowley, T. Mckinnon, E. Kowalska, V. Sluka, A. M. Deac, B. Heinrich, and E. Girt, Spin torque switching in nanopillars with antiferromagnetic reference layer, IEEE Magn. Lett. **8**, 1 (2017).

[9] M. Arora, N. R. Lee-Hone, T. Mckinnon, C. Coutts, R. Hübner, B. Heinrich, D. M. Broun, and E. Girt, Magnetic properties of Co/Ni multilayer structures for use in STT-RAM, J. Phys. D: Appl. Phys. **50**, 505003 (2017).

[10] B. Dieny and M. Chshiev, Perpendicular magnetic anisotropy at transition metal/oxide interfaces and applications, Rev. Mod. Phys. **89**, 025008 (2017).

[11] S. Zoll, H. A. M. Van den Berg, J. P. Jay, H. J. Elmers, C. Meny, P. Panissod, D. Stoeffler, A. Dinia, and K. Ounadjela, Coupling mechanism in Co/Ru sandwiches with thin spacers, J. Magn. Magn. Mater. **156**, 231 (1996),proceedings of the Second International Symposium on Metallic Multilayers.

[12] S. Zoll, A. Dinia, J. P. Jay, C. Mény, G. Z. Pan, A. Michel, L. El Chahal, V. Pierron-Bohnes, P. Panissod, and H. A. M. van den Berg, Influence of the growth technique on the coupling and magnetoresistance of Co/Ru sandwiches, Phys. Rev. B **57**, 4842 (1998).

[13] A. Dinia, S. Zoll, M. Gester, D. Stoeffler, J. P. Jay, K. Ounadjela, H. A. M. van den Berg, and H. Rakoto, Interfacial polarisation effect on the interlayer couplings in Co/Rh sandwiches, Eur. Phys. J. B—Condens. Matter Complex Syst. **5**, 203 (1998).

[14] S. Zoll, A. Dinia, D. Stoeffler, M. Gester, H. A. M. van den Berg, and K. Ounadjela, Preserved interfacial magnetism and giant antiferromagnetic exchange coupling in Co/Rh sandwiches, EPL **39**, 323 (1997).

[15] J. Chatterjee, R. C. Sousa, N. Perrissin, S. Auffret, C. Ducruet, and B. Dieny, Enhanced annealing stability and perpendicular magnetic anisotropy in perpendicular magnetic tunnel junctions using W layer, Appl. Phys. Lett. **110**, 202401 (2017).

[16] K. Yakushiji, A. Fukushima, H. Kubota, M. Konoto, and S. Yuasa, Ultralow-voltage spin-transfer switching in perpendicularly magnetized magnetic tunnel junctions with synthetic antiferromagnetic reference layer, Appl. Phys. Express **6**, 113006 (2013).

[17] S. N. Okuno and K. Inomata, Dependence on Fermi surface dimensions of oscillatory exchange coupling in $Co/Cu_{1-x}Ni_x(110)$ multilayers, Phys. Rev. Lett. **70**, 1711 (1993).

[18] S. S. P. Parkin, C. Chappert, and F. Herman, Oscillatory exchange coupling and giant magnetoresistance via Cu-X alloys ($X =$ Au, Fe, Ni), Europhys. Lett. (EPL) **24**, 71 (1993).

[19] P. Bruno and C. Chappert, Oscillatory coupling between ferromagnetic layers separated by a nonmagnetic metal spacer, Phys. Rev. Lett. **67**, 1602 (1991).

[20] P. Bruno, Physical mechanism of oscillatory interlayer exchange coupling, J. Magn. Magn. Mater. **116**, L13 (1992).

[21] Z. R. Nunn, C. Abert, D. Suess, and E. Girt, Control of the noncollinear interlayer exchange coupling, Sci. Adv. **6**, eabd8861 (2020).

[22] J. Lisik, S. Myrtle, and E. Girt, Noncollinear interlayer exchange coupling across IrFe spacer layers, J. Magn. Magn. Mater. **585**, 171109 (2023).

[23] Z. R. Nunn, J. Lisik, P. Omelchenko, S. Koraltan, C. Abert, D. Suess, and E. Girt, Controlling the angle between magnetic moments of Co layers in Co|RuCo|Co, J. Appl. Phys. **133**, 123901 (2023).

[24] P. Franke and D. Neuschütz, in *Landolt-Börnstein Numerical Data and Functional Relationships in Science and Technology: Group IV: Physical Chemistry* (Springer Berlin, Heidelberg, 2007), Vol. 19B5.

[25] E. Goering, S. Gold, A. Bayer, and G. Schuetz, Non-symmetric influences in the total electron yield x-ray magnetic circular dichroism signal in applied magnetic fields, J. Synchrotron. Radiat. **8**, 434 (2001).

[26] P. Carra, B. T. Thole, M. Altarelli, and X. Wang, X-ray circular dichroism and local magnetic fields, Phys. Rev. Lett. **70**, 694 (1993).

[27] B. T. Thole, P. Carra, F. Sette, and G. van der Laan, X-ray circular dichroism as a probe of orbital magnetization, Phys. Rev. Lett. **68**, 1943 (1992).

[28] C. T. Chen, Y. U. Idzerda, H. J. Lin, N. V. Smith, G. Meigs, E. Chaban, G. H. Ho, E. Pellegrin, and F. Sette, Experimental confirmation of the X-ray magnetic circular dichroism sum rules for iron and cobalt, Phys. Rev. Lett. **75**, 152 (1995).

[29] V. Chakarian and Y. U. Idzerda, Total electron yield method in X-ray absorption spectroscopy: A closer look at the saturation/self-absorption effects (abstract), J. Appl. Phys. **81**, 4709 (1997).

[30] R. Nakajima, J. Stöhr, and Y. U. Idzerda, Electron-yield saturation effects in l-edge x-ray magnetic circular dichroism spectra of Fe, Co, and Ni, Phys. Rev. B **59**, 6421 (1999).

[31] G. Kresse and J. Furthmüller, Efficient iterative schemes for ab initio total-energy calculations using a plane-wave basis set, Phys. Rev. B **54**, 11169 (1996).

[32] G. Kresse and D. Joubert, From ultrasoft pseudopotentials to the projector augmented-wave method, Phys. Rev. B **59**, 1758 (1999).

[33] P. E. Blöchl, Projector augmented-wave method, Phys. Rev. B **50**, 17953 (1994).

[34] J. P. Perdew, K. Burke, and M. Ernzerhof, Generalized gradient approximation made simple, Phys. Rev. Lett. **77**, 3865 (1996).

[35] H. J. Monkhorst and J. D. Pack, Special points for Brillouin-zone integrations, Phys. Rev. B **13**, 5188 (1976).

[36] M. Methfessel and A. T. Paxton, High-precision sampling for Brillouin-zone integration in metals, Phys. Rev. B **40**, 3616 (1989).

[37] R. P. Feynman, Forces in molecules, Phys. Rev. **56**, 340 (1939).

[38] P. Vinet, J. R. Smith, J. Ferrante, and J. H. Rose, Temperature effects on the universal equation of state of solids, Phys. Rev. B **35**, 1945 (1987).

[39] See Supplemental Material at http://link.aps.org/supplemental/10.1103/PhysRevApplied.22.024058 for 3×3 structure results and additional atomic structures utilized in the presented calculations.

[40] C. Eyrich, A. Zamani, W. Huttema, M. Arora, D. Harrison, F. Rashidi, D. Broun, B. Heinrich, O. Mryasov, M. Ahlberg, O. Karis, P. E. Jönsson, M. From, X. Zhu, and E. Girt, Effects of substitution on the exchange stiffness and magnetization of co films, Phys. Rev. B **90**, 235408 (2014).

[41] M. D. Stiles, in *Ultrathin Magnetic Structures III: Fundamentals of Nanomagnetism*, edited by J. A. C. Bland and B. Heinrich (Springer Berlin Heidelberg, Berlin, Heidelberg, 2005), p. 99.

[42] P. J. H. Bloemen, M. T. Johnson, M. T. H. van de Vorst, R. Coehoorn, J. J. de Vries, R. Jungblut, J. aan de Stegge, A. Reinders, and W. J. M. de Jonge, Magnetic layer thickness dependence of the interlayer exchange coupling in (001) Co/Cu/Co, Phys. Rev. Lett. **72**, 764 (1994).

[43] M. D. Stiles, Exchange coupling in magnetic heterostructures, Phys. Rev. B **48**, 7238 (1993).

[44] P. Bruno, Theory of interlayer magnetic coupling, Phys. Rev. B **52**, 411 (1995).

[45] T. Mckinnon, B. Heinrich, and E. Girt, Spacer layer thickness and temperature dependence of interlayer exchange coupling in Co/Ru/Co trilayer structures, Phys. Rev. B **104**, 024422 (2021).

[46] Z. R. Nunn and E. Girt, Non-collinear coupling across RuCo and RuFe alloys, arXiv:1901.07055 [cond-mat.mtrl-sci].

[47] E. Girt and H. J. Richter, Antiferromagnetically coupled perpendicular recording media, IEEE Trans. Magn. **39**, 2306 (2003).

[48] C. Eyrich, A. Zamani, W. Huttema, M. Arora, D. Harrison, F. Rashidi, D. Broun, B. Heinrich, O. Mryasov, M. Ahlberg, O. Karis, P. E. Jönsson, M. From, X. Zhu, and E. Girt, Effects of substitution on the exchange stiffness and magnetization of Co films, Phys. Rev. B **90**, 235408 (2014).

Correction: The value given for A in the first sentence of the caption of Figure 2 was incorrect and has been fixed. The previously published Figure 4 contained incorrect units and has been replaced.